

New 3D coded aperture collimator for X/gamma-ray wide-field imaging

Yaroslav Susaiev^{1,*}, Vincent Schoepff¹, Olivier Limousin²

¹Université Paris-Saclay, CEA, List, F-91120 Palaiseau, France

²Université Paris-Saclay, CEA, Irfu, F-91191 Gif-sur-Yvette, France

(*) yaroslav.susaiev@cea.fr

Abstract—Remote localization of radioactive sources is vital to the nuclear industry and high-energy astrophysics. One widely used method to localize radioactive sources relies on indirect imaging with coded aperture cameras. It involves using a coded aperture collimator called the “coded mask” accompanied by a position-sensitive X/gamma-ray detector with a dedicated deconvolution algorithm. However, a known disadvantage of such cameras is their limited field of view, resulting in a restricted capture area when analyzing complex contaminated scenes or transient astrophysical events. Our paper introduces a new non-planar coded mask prototype designed to expand the field of view of standard coded aperture cameras. Our 3D coded mask is a tantalum hemisphere with a spiral-shaped hole. We use the Maximum Likelihood Expectation Maximization algorithm to reconstruct the radioactive source images. We test our prototype on data acquired with Timepix3 hybrid pixel detector equipped with our mask.

Keywords —Gamma imaging, 3D coded mask, Timepix3

I. INTRODUCTION

Remote localization of radioactive sources is a crucial challenge in nuclear instrumentation physics, with different applications ranging from the nuclear industry [1,2] to high-energy astrophysics [3,4]. Identifying radioactive source position and intensity in complex contaminated scenes is gaining significant relevance following the Fukushima nuclear disaster in Japan and the recent Zaporizhzhia Nuclear Power Plant occupation in Ukraine.

Localization of radioactive sources by direct imaging using compact systems of lenses and mirrors is not feasible due to the fundamental nature of X/gamma-ray photons. Fortunately, indirect imaging methods offer commonly used solutions, with two primary approaches available: Compton imaging and coded aperture imaging. The first approach relies on the Compton scattering phenomenon and can be applied to image radioactive sources of energies above 250 keV [5]. This method benefits from a wide field of view from 2π to 4π steradians while being capable of providing an angular resolution of approximately 10° . This paper focuses on the second approach of coded aperture imaging, which allows for imaging radioactive sources across a wide energy range, from a few keV to several MeV [6]. Historically, this method originates from the classical pinhole camera, and its idea is as follows. A coded

aperture mask, a multi-pinhole collimator, modulates the X/gamma-ray photon flux emitted by a radioactive source. The opaque elements of the mask absorb the incoming X/gamma rays, while the transparent elements (holes) allow them to pass through. After, the holes cast the shadow of the mask pattern onto the detector plane called the “shadowgram”. Finally, we can decode the shadowgram using deconvolution algorithms to obtain the reconstructed image of the radioactive source.

There is a wide variety of different coded mask patterns, such as Uniformly Redundant Arrays (URAs) [7], Modified Uniformly Redundant Arrays (MURAs) [8], and random arrays [9,10]. These patterns are primarily used in coded masks of planar geometries, limiting corresponding imaging characteristics. In principle, for a given position of a point source of photons in space, any unambiguous pattern projecting a unique shadowgram onto the detector can be considered to create a coded mask. Of course, the pattern design depends on various factors, such as observed flux intensity, photon energy, background noise, and mathematical reconstruction methods. Usually, coded aperture cameras equipped with the planar coded masks feature a field of view up to $50^\circ \times 50^\circ$ and an angular resolution above 1° . Table I provides the parameters of some existing X/gamma-ray imaging systems.

TABLE I
 CHARACTERISTICS OF EXISTING X/GAMMA-RAY IMAGING SYSTEMS

Imaging system	Mask type	Field of view	Angular resolution
Integral / IBIS [11]	Random	$29.1^\circ \times 29.4^\circ$	0.2° (12 arcmin)
iPIX [12]	MURA	$48.8^\circ \times 48.8^\circ$	2.5° (150 arcmin)
NuVISION [2]	MURA	$45.0^\circ \times 45.0^\circ$	3.5° (210 arcmin)
Nanopix [13]	MURA	$48.8^\circ \times 48.8^\circ$	2.5° (150 arcmin)
SpidX [14]	Random	$55.0^\circ \times 55.0^\circ$	1.0° (60 arcmin)
SVOM / Eclairs [4]	Random	$90.0^\circ \times 90.0^\circ$	0.5° (30 arcmin)

Therefore, the ideal coded aperture camera would have a field of view as wide as 2π steradians and an angular resolution of less than 1° , which is practically unachievable with currently available technologies. Noteworthy endeavors to reach these parameters can be found in literature, such as radial hole coded masks [15], rotating scatter masks [16], and active coded masks [17].

Our research introduces a novel method based on a non-planar coded mask aperture system called the “3D coded mask”. Its primary objective is to achieve nearly 2π steradians field of view with a single planar position sensitive detector while maintaining an angular resolution in the range of the state-of-the-art systems as in Table I. We manufactured the first

3D coded mask by the tantalum machining process. To reconstruct radioactive sources in a wide field of view, we apply a deconvolution algorithm that relies on a database of the mask pattern projections (the “projectors”) explicitly generated for our geometry using an analytical approach.

The paper is structured as follows. Section II introduces the 3D coded mask, its characteristics, and expected performance. Section III describes the camera prototype based on the 3D coded aperture equipped with the Timepix3 hybrid-pixel detector. Section IV describes the method of generating the projection dataset specific to our mask, which is later used in Sections V and VI to analyze the simulation and experimental results.

II. 3D CODED MASK

Our 3D coded mask is a tantalum hemisphere with a spiral-shaped hole. Its unique design aims to show how an unambiguous arbitrary mask pattern can provide a wide field of view of nearly 2π steradians. The mask is presented in Fig. 1.

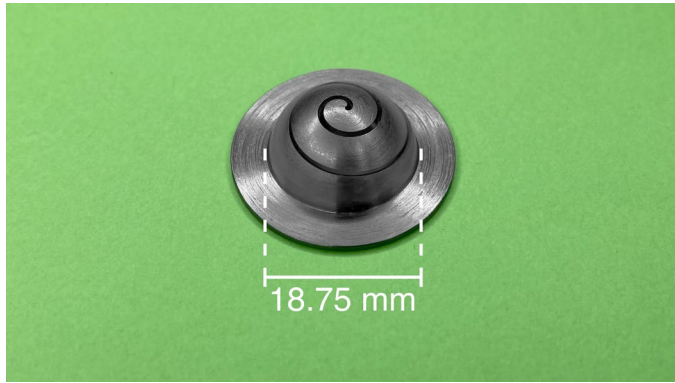


Fig. 1. Picture of the 3D coded mask.

The 3D coded mask is manufactured by tantalum machining process, which offers precise cutting and shaping of the metal. Tantalum is often used as coded mask material due to its capability of absorbing high-energy photons. With its high atomic number ($Z = 73$) and density ($D = 16.69 \text{ g/cm}^3$), the total probability of shielding the ^{241}Am 59.54 keV photons by the opaque elements of the mask is 99%.

The opaque elements of the mask form a hemispherical shape. Such geometry ensures the uniform mask surface illumination by X/gamma rays coming from any direction in the sky. The diameter of the hemisphere is 18.75 mm, or 28 mm in total, including the outer brim. The latter is used to fasten the aperture in front of the detector accurately. The mask has a thickness of 0.75 mm, matching the width of the spiral hole.

The transparent elements of the mask form a continuous opening that has a shape of a one-arm Archimedean spiral. The reason for choosing this unique pattern geometry was to achieve significant pattern asymmetry while retaining the manufacturing advantages of a continuous hole, thus simplifying the initial phase of our work. Mathematically, the Archimedean spiral can be defined by (1) in polar coordinates.

$$r = a + b\theta = a + \frac{1}{2\pi n_t} \cdot \theta \quad (1)$$

Here, a and b are real numbers, and n_t is the number of successive turns of the spiral. By design of our mask pattern, $a = 0$ and $n_t = 2.5$. Then the Archimedean spiral equation represented by (1) takes the form (2).

$$r = \frac{1}{5\pi} \cdot \theta \quad (2)$$

Table II summarizes the parameters of the 3D coded mask spiral pattern.

TABLE II
PARAMETERS OF THE 3D CODED MASK SPIRAL PATTERN

Parameter	3D CODED MASK
Pattern geometry	Hemispherical Archimedean spiral
Number of spiral arms	1
Number of spiral turns (n_t)	2.5
Spiral diameter	16.875 mm
Spiral hole width	0.75 mm
Open fraction	10.2%

III. TIMEPIX3 CAMERA PROTOTYPE

We developed an ultra-compact X/gamma-ray coded aperture camera prototype equipped with the 3D coded mask to conduct measurements of radioactive sources in a wide field of view. The camera is based on state of the art Timepix3 photon sensor, a part of the Timepix family of hybrid pixel detectors developed in the frame of the Medipix3 collaboration at CERN [18]. In our work, we utilize a Timepix3 interface called MiniPIX TPX3 designed by Advacam. It is a small $77 \text{ mm} \times 21 \text{ mm} \times 10 \text{ mm}$ device with an ARM processor and USB interface for data pre-processing and readout.

Timepix3 is $14.08 \text{ mm} \times 14.08 \text{ mm}$ large, with a 1 mm thick cadmium telluride crystal. The detector features a high pixel resolution matrix with a 256×256 pixels detection surface and $55 \mu\text{m}$ pixel pitch. Timepix3 can operate in two modes simultaneously: Time-over-Arrival, which provides the particle arrival time, and Time-over-Threshold, which records the particle deposited energy. This work focuses on the second mode when collecting data.

To assemble the X/gamma-ray camera, we position our 3D coded mask in front of the Timepix3 detection surface, ensuring alignment along the axis that intersects the mask zenith and the detector center. The mask should be placed directly on top of the detector to provide the maximum field of view, with the upper detection plane being coplanar with the mask brim. In such a setup, the camera only has the fully coded field of view when the coded aperture fully modulates the photon flux.

However, in our camera setup, this ideal configuration is not achievable due to the MiniPIX TPX3 plastic body, which creates a gap between the upper detection plane and the 3D coded mask brim. This configuration is illustrated in Fig. 2.

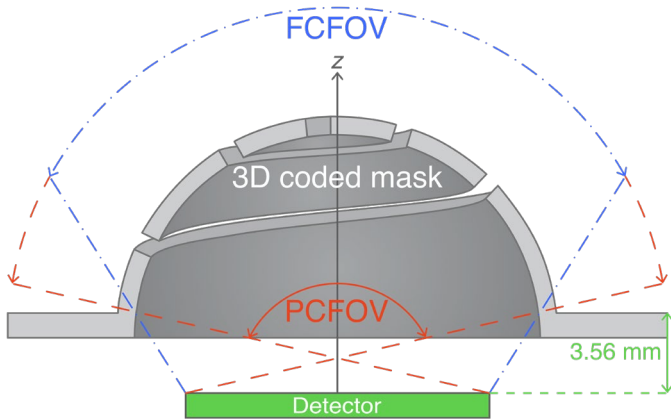


Fig. 3. Illustration of the 3D coded mask camera setup (side view). FCFOV stands for “fully coded field of view” (blue-colored range), and PCFOV corresponds to “partially coded field of view” (red-colored range).

The smallest gap between the mask and the detector is 3.56 mm, resulting in a reduced field of view. In such an imaging system, we have the partially coded field of view, including the observation range when the mask modulates the photon flux only partially.

From geometrical considerations, the maximum field of view of our Timepix3-based camera is $154.3^\circ \times 154.3^\circ$. However, the effective field of view is not constant and depends on the spiral hole orientation to the observable source. According to the mask hole width, the detector pixel pitch, and mask-to-detector distance (radius of the mask and the gap), the best angular resolution achievable by our camera is 3.5° . However, the spiral hole is continuous along in azimuth direction but segmented in polar. Thus, our X/gamma camera has two distinct angular resolutions, azimuthal and polar, which also depend on the reconstruction algorithm.

IV. PROJECTION DATASET AND RECONSTRUCTION ALGORITHM

Projection datasets are essential in reconstructing radioactive source shadowgrams captured by the 3D coded mask camera. In planar coded aperture imaging systems, the traditional reconstruction procedure relies on a single projection of the whole mask pattern onto the detection plane, representing the mask pattern itself. However, when the mask geometry is not planar, every position of the observable source in the sky is associated with a projection onto the detector plane that has to be carefully calculated.

To address this issue, we developed a Python code that provides spiral pattern projections for any given position of the source in the sky from an analytical description. Given the 3D model of our mask, the code generates orthogonal projections of the spiral hole onto the detector surface. The algorithm is not Monte Carlo-based, offering the flexibility of altering the 3D coded mask geometry and a fast computation time. Fig. 3 shows the projectors generated for two different positions of the observable source.

The trade-off is the somewhat simplified model, where the 3D coded mask is infinitely thin. Therefore, the absence of the vignetting effect might bias the reconstruction as the effective open fraction of the 3D coded aperture is smaller in reality than

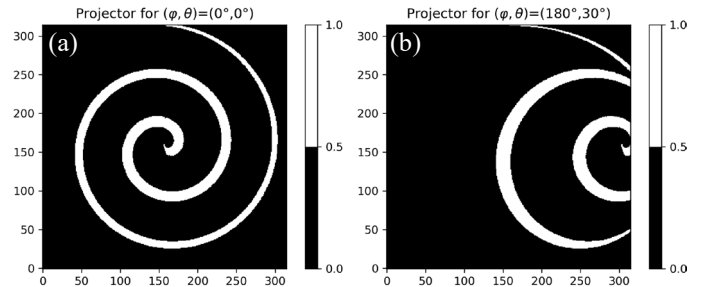


Fig. 2. Mathematical projections of the spiral pattern onto the detector plane for two different positions of a photon source in the sky: (a) observable source is in front of the camera, (b) source is shifted on the zenith angle of 30° .

in the model. The model also does not consider the attenuation or scattering effects in the projectors. The projection datasets generated by the code are later used for reconstruction and detector response simulation.

Reconstructing radioactive sources involves solving an inverse problem, where the goal is to decode the original image from the encoded image represented by a detector response. For this purpose, we use the Maximum Likelihood Expectation Maximization (MLEM) algorithm, which conveniently relies on projection datasets independent from the mask pattern geometry. MLEM is an iterative algorithm initially developed for tomographic reconstruction [19], which iteratively maximizes the probability $p(D|S)$ of observing detector response D provided the reconstructed image S . For each iteration n , the update formula for the optimal image \hat{S} is given by (3).

$$\hat{S}_j^{n+1} = \hat{S}_j^n \sum_i \frac{p(i|j)D_i}{\sum_{j'} p(i|j')\hat{S}_{j'}^n} \quad (3)$$

Here, $p(i|j)$ is the probability of detecting a photon emitted from sky pixel j in the detector pixel i . With each iteration of MLEM, the resulting image quality increases at the cost of the computational time, which may be impractical when real-time radioactive source reconstruction is required.

V. SIMULATIONS WITH THE 3D CODED MASK

Now we can simulate the Timepix3 detector response using the previously generated projection dataset. In our model, we define the photon source position in the sky using the horizontal coordinate system (θ, φ) , where θ is the zenith angle, and φ is the azimuth angle. Choosing the zenith angle over the polar allows us to define the zenith point at $(\theta, \varphi) = (0^\circ, 0^\circ)$. Photon counts are simulated by filling the projections with Poisson distribution $\text{Pois}(\lambda)$, where λ is a real number that corresponds to the number of counts N in a specific time interval. In the model, N also depends on the source zenith angle and follows a cosine-squared law $N = \cos^2(\theta)$. The number of counts is maximum when the photon source is in the camera zenith.

Fig. 4 shows the simulated Timepix3 responses alongside the corresponding MLEM reconstruction of a far-field point source located at two positions: $(\varphi_1, \theta_1) = (180^\circ, 15^\circ)$, and $(\varphi_2, \theta_2) = (180^\circ, 45^\circ)$. The number of registered counts is

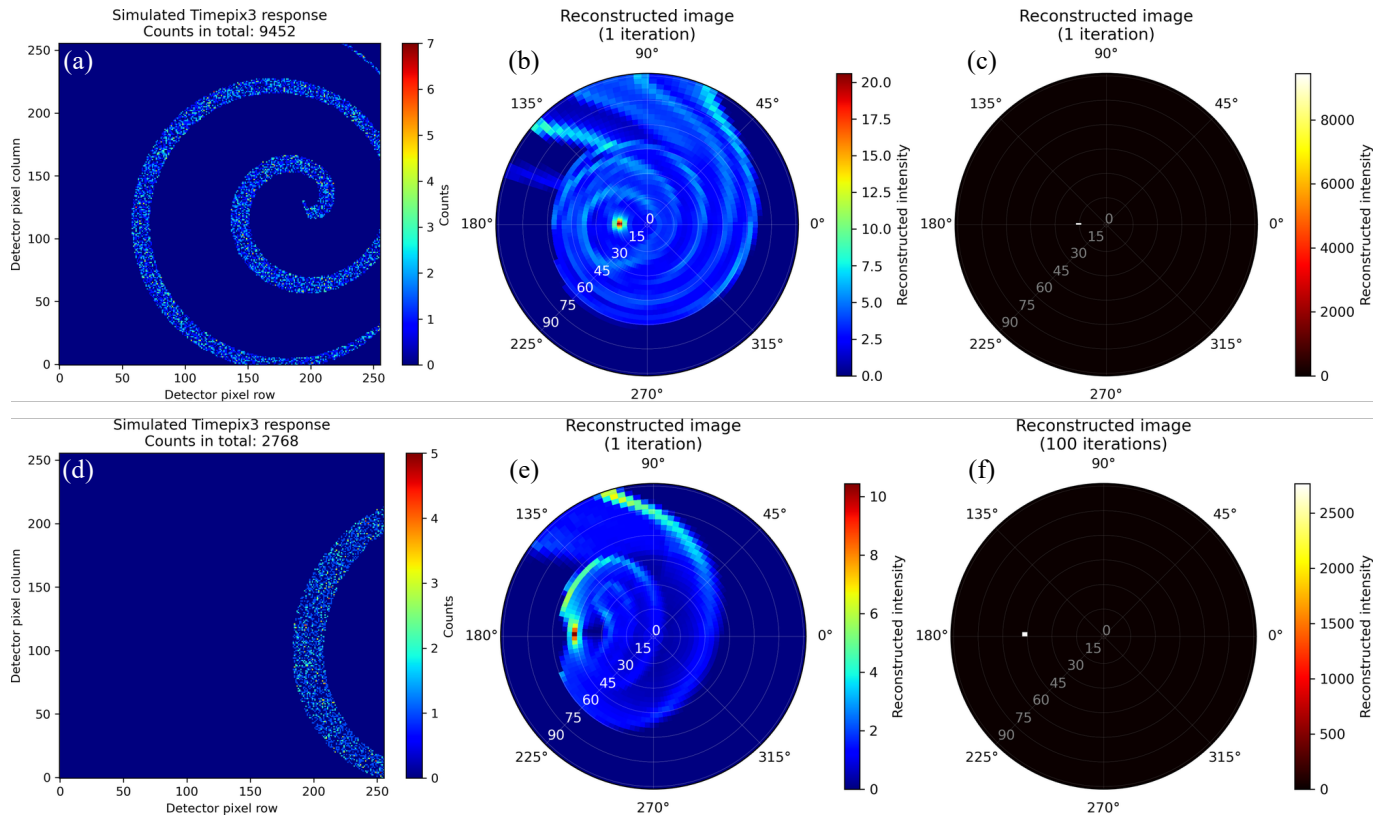


Fig. 4. Simulated Timepix3 responses (a),(d) alongside with the reconstructed images obtained by MLEM after 1 iteration (b),(e) and 100 iterations (c),(f). The top row corresponds to $(\theta_1, \varphi_1) = (180^\circ, 15^\circ)$, and the bottom row to $(\theta_2, \varphi_2) = (180^\circ, 45^\circ)$. The reconstructed images are discretized with $120^\circ \times 30^\circ$ positions, where each pixel corresponds to the angle of 3° .

9452 and 2768 for the camera at $(\theta_1, \varphi_1) = (180^\circ, 15^\circ)$ and $(\theta_2, \varphi_2) = (180^\circ, 45^\circ)$, respectively. MLEM localized the observable source at its true position for both simulations.

Fig. 4e shows that the reconstructed noise becomes more substantial with the observable source moving further from the zenith along the polar direction. With no additional simulated background, this noise is intrinsic to our 3D coded aperture imaging system due to the uneven effective open fraction of the mask. Indeed, when the detector response is represented only by the arc-shaped part of the spiral pattern, as in Fig. 4d, the MLEM algorithm attributes it to more than a single projector and generates noise. If the observable source is located at the zenith angles $\theta > 30^\circ$, we can improve the imaging quality by performing more MLEM iterations to reach an almost noise-free image (Fig. 4f) or by rotating the mask to a more favorable position featuring more explicit spiral shadow (Fig. 4a).

VI. MEASUREMENTS WITH THE 3D CODED MASK

We conducted a series of measurements with the Timepix3 camera equipped with the 3D coded mask to compare the acquired data with the simulations. In these measurements, we observed a single ^{241}Am source with an activity of 74 MBq, which was placed one meter away from the camera at two positions: $(\theta_1, \varphi_1) = (180^\circ, 15^\circ)$ and $(\theta_2, \varphi_2) = (180^\circ, 45^\circ)$. Such a setup is similar to the simulated examples in Fig 4. The acquisition time is 100 seconds at one frame per second. The number of registered counts is 63293 and 41162 for the

observable source located in $(\theta_1, \varphi_1) = (180^\circ, 15^\circ)$ and $(\theta_2, \varphi_2) = (180^\circ, 45^\circ)$, respectively.

Fig. 5 shows the Timepix3 responses and the associated MLEM reconstruction images after 1 and 100 iterations. The algorithm localized the ^{241}Am source at its actual position for both measurements.

We observe that the reconstructed source is elongated in Fig. 5e, roughly three pixels wide in azimuth. While the setup alignment is supposed to be perfect in the measurement, a slight shift of the radioactive source affects the reconstruction quality. In addition, neglecting the vignetting effect in the projector database might also contribute to this uncertainty and will be studied further in future works. Thus, the observed inequality between the angular resolutions justifies the need to attribute two angular resolutions to our mask, azimuthal and polar. These parameters also depend on the observable source position and the reconstruction algorithm. According to these data, the angular width of the point spread function after 100 MLEM iterations is approximately 3° in the zenith angle as expected, and 9° in the azimuth angle.

VII. CONCLUSIONS

A hemispherical coded mask with a spiral-shaped hole was developed and characterized with a single Timepix3 chip. We aimed to demonstrate how the traditional limitations of standard

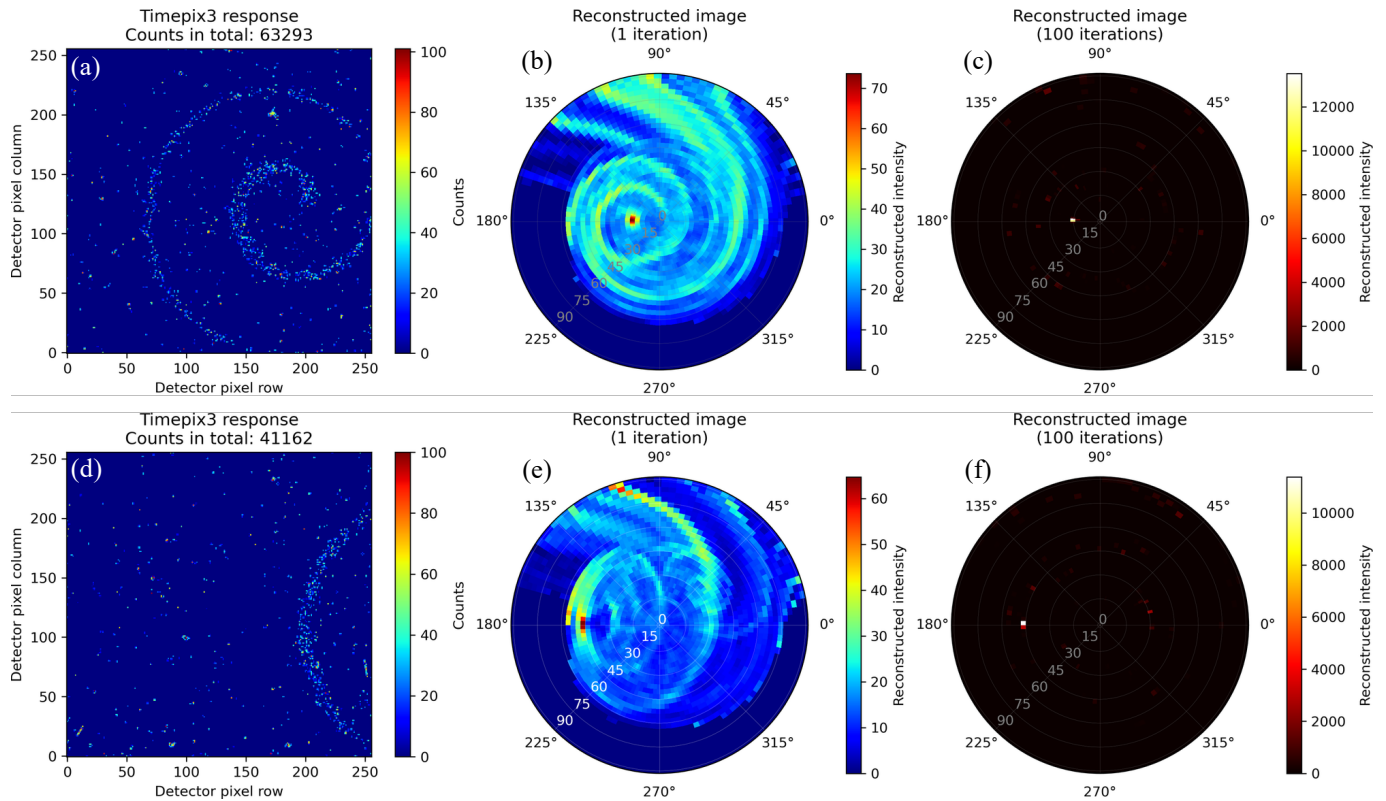


Fig. 5. Measured Timepix3 responses (a),(d) obtained after 100 seconds of data acquisition with ^{241}Am (74 MBq) alongside with the reconstructed images obtained by MLEM after 1 iteration (b),(e) and 100 iterations (c),(f). The top row corresponds to $(\theta_1, \varphi_1) = (180^\circ, 15^\circ)$, and the bottom row to $(\theta_2, \varphi_2) = (180^\circ, 45^\circ)$. The reconstructed images are discretized with $120^\circ \times 30^\circ$ positions, where each pixel corresponds to the angle of 3° . Finally, we apply an upper threshold of 100 counts to (a),(d) to cover the noise.

X/gamma-ray cameras can be addressed using a non-planar coded mask with an unambiguous pattern.

Our imaging system has demonstrated accurate localization capability within the effective field of view up to $90^\circ \times 90^\circ$ according to the analytical simulations with a far-field point source and measurements with ^{241}Am with the activity of 74 MBq. Such camera holds potential for use in the nuclear industry and high-energy astrophysics applications, particularly when the radioactive source location is unknown.

We have effectively implemented the MLEM algorithm to reconstruct the images of radioactive sources. The zenith angle increase results in more prominent artifacts and increased azimuthal angular resolution, thus affecting the source localization precision. A higher number of MLEM iterations or an additional measurement with the 3D coded mask rotation can partially solve this issue. The uneven effective open fraction of the one-arm spiral pattern also affects the quality of reconstruction. It signifies the need of further aperture pattern optimization.

Future work will focus on the next 3D coded mask design and development, which features an enhanced coded pattern and geometrical characteristics aiming to overcome the imperfections of its predecessor. We plan to optimize the projector generation and reconstruction codes as we move forward. Finally, we anticipate conducting simulations and measurements with several radioactive sources of different activities.

REFERENCES

- [1] F. Carrel *et al.*, “GAMPIX: A new gamma imaging system for radiological safety and Homeland Security Purposes,” in *2011 IEEE Nuclear Science Symposium Conference Record*, Valencia, Spain: IEEE, Oct. 2011, pp. 4739–4744. doi: 10.1109/NSSMIC.2011.6154706.
- [2] G. Montemont *et al.*, “NuVISION: a Portable Multimode Gamma Camera based on HiSPECT Imaging Module,” in *2017 IEEE Nuclear Science Symposium and Medical Imaging Conference (NSS/MIC)*, Atlanta, GA: IEEE, Oct. 2017, pp. 1–3. doi: 10.1109/NSSMIC.2017.8532713.
- [3] F. Lebrun *et al.*, “ISGRI: The INTEGRAL Soft Gamma-Ray Imager,” *Astron. Astrophys.*, vol. 411, no. 1, pp. L141–L148, Nov. 2003, doi: 10.1051/0004-6361:20031367.
- [4] O. Godet *et al.*, “The X-/Gamma-ray camera ECLAIRS for the Gammay-ray burst mission SVOM,” 2014, doi: 10.48550/ARXIV.1406.7759.
- [5] C. G. Wahl *et al.*, “The Polaris-H imaging spectrometer,” *Nucl. Instrum. Methods Phys. Res. Sect. Accel. Spectrometers Detect. Assoc. Equip.*, vol. 784, pp. 377–381, Jun. 2015, doi: 10.1016/j.nima.2014.12.110.
- [6] R. Accorsi, “Design of a near-field coded aperture cameras for high-resolution medical and industrial gamma-ray imaging,” Thesis, Massachusetts Institute of

- Technology, 2001. Accessed: Dec. 16, 2022. [Online]. Available: <https://dspace.mit.edu/handle/1721.1/8684>
- [7] E. E. Fenimore and T. M. Cannon, "Coded aperture imaging with uniformly redundant arrays," *Appl. Opt.*, vol. 17, no. 3, p. 337, Feb. 1978, doi: 10.1364/AO.17.000337.
- [8] S. R. Gottesman and E. E. Fenimore, "New family of binary arrays for coded aperture imaging," *Appl. Opt.*, vol. 28, no. 20, p. 4344, Oct. 1989, doi: 10.1364/AO.28.004344.
- [9] R. H. Dicke, "Scatter-Hole Cameras for X-Rays and Gamma Rays," *Astrophys. J.*, vol. 153, p. L101, Aug. 1968, doi: 10.1086/180230.
- [10] J. G. Ables, "Fourier Transform Photography: A New Method for X-Ray Astronomy," *Publ. Astron. Soc. Aust.*, vol. 1, no. 4, pp. 172–173, Dec. 1968, doi: 10.1017/S1323358000011292.
- [11] P. Ubertini *et al.*, "IBIS: The Imager on-board INTEGRAL," *Astron. Astrophys.*, vol. 411, no. 1, pp. L131–L139, Nov. 2003, doi: 10.1051/0004-6361:20031224.
- [12] K. Amgarou *et al.*, "A comprehensive experimental characterization of the iPIX gamma imager," *J. Instrum.*, vol. 11, no. 08, pp. P08012–P08012, Aug. 2016, doi: 10.1088/1748-0221/11/08/P08012.
- [13] V. Schoepff *et al.*, "Nanopix, a smart and highly miniaturized gamma camera for robotic radiological characterization," presented at the SFEN DEM 2021 – International Conference on Decommissioning Challenges: Industrial Reality, Lessons learned and Prospects, Avignon, France, Jun. 2021.
- [14] R. Le Breton *et al.*, "The Spid-X gamma camera: A miniature gamma ray integral field spectrometer for nuclear industry applications," *Nucl. Instrum. Methods Phys. Res. Sect. Accel. Spectrometers Detect. Assoc. Equip.*, vol. 1047, p. 167722, Feb. 2023, doi: 10.1016/j.nima.2022.167722.
- [15] J. E. Grindlay and J. Hong, "Optimizing wide-field coded aperture imaging: radial mask holes and scanning," presented at the Optical Science and Technology, SPIE's 48th Annual Meeting, O. Citterio and S. L. O'Dell, Eds., San Diego, California, USA, Jan. 2004, p. 402. doi: 10.1117/12.506260.
- [16] J. G. M. FitzGerald, "A Rotating Scatter Mask for Inexpensive Gamma-Ray Imaging in Orphan Source Search: Simulation Results," *IEEE Trans. Nucl. Sci.*, vol. 62, no. 1, pp. 340–348, Feb. 2015, doi: 10.1109/TNS.2014.2379332.
- [17] D. Hellfeld, P. Barton, D. Gunter, L. Mihailescu, and K. Vetter, "A Spherical Active Coded Aperture for π Gamma-Ray Imaging," *IEEE Trans. Nucl. Sci.*, vol. 64, no. 11, pp. 2837–2842, Nov. 2017, doi: 10.1109/TNS.2017.2755982.
- [18] T. Poikela *et al.*, "Digital column readout architectures for hybrid pixel detector readout chips," *J. Instrum.*, vol. 9, no. 01, pp. C01007–C01007, Jan. 2014, doi: 10.1088/1748-0221/9/01/C01007.
- [19] L. A. Shepp and Y. Vardi, "Maximum Likelihood Reconstruction for Emission Tomography," *IEEE Trans. Med. Imaging*, vol. 1, no. 2, pp. 113–122, Oct. 1982, doi: 10.1109/TMI.1982.4307558.